Electromagnetic Interference Effect Assessment Under Measuring Testability Limitation Based on Physics-Informed Neural Network and Gaussian Process Regression

Wenchao Lu, *Student Member, IEEE*, Jiandong Duan, *Member, IEEE*, Lin Cheng, Jiangping Lu, and Dongxing Dou

***Abstract*—The transient electromagnetic interference in practical existing engineering have measuring testability limitation. This limitation makes it difficult to assess electromagnetic effect. A multidimensional physical information based assessment method via physics-informed neural network (PINN) and Gaussian process regression (GPR) is proposed in this article. First, the physical topology of the disturbed equipment under electromagnetic interference is analyzed, and the partial differential equation of the space electric field is derived from the measurable electric quantity. Then, the electric field near the disturbed equipment is predicted by PINN which can characterize the physical information. Finally, combining calculated electric field data and measured magnetic field data, a two-dimensional GPR regression is used to assess the electromagnetic effect with multiple inputs and outputs, and the probabilities under each state are then calculated based on the assessed state. Expanded verification is conducted by combining different electromagnetic complexity calculation methods, proving the applicability and effectiveness of the proposed assessment model.**

***Index Terms*—Electromagnetic interference, effect assessment, intelligent measurement equipment, gaussian process regression (GPR), physics-informed neural network (PINN).**

I. Introduction

AT PRESENT, the intelligent measurement equipment in the substation is vulnerable to electromagnetic interference, which threatens the safe operation of the power system. Typically, there is no recording device specifically designed for transient disturbance in the substation, which makes it difficult for on-site engineers to identify the cause of the interference. Furthermore, the lack of available failure data for interference assessment is due to the randomness of electromagnetic interference problems and the confidentiality principle of substation accidents. Simulated interference tests either cannot restore the interference scenario (usually, it takes hundreds of times the interference intensity under actual conditions to trigger failure effect [1], [2], [3]), or the equipment is too expensive that the cost of interference damage cannot be borne. Therefore, it is extreme important to evaluate the electromagnetic interference effect under the measuring testability limitation of equipment.

Scholars have done a lot of work on data acquisition of electromagnetic interference, including laboratory simulation tests and measurement tests in actual substations. One part is represented by interference measurements of flexible ac transmission systems (FACTS) equipment in substations [4], such as laboratory radiation interference when insulated gate bipolar transistor (IGBT) switches are turned ON [5], electromagnetic interference of IGBT internal oscillations to themselves [6], and transient electric field measurements during the operation of modular multilevel converter (MMC) and high-voltage dc circuit breakers [7]. The other part mainly lies in the interference and measurement of intelligent electronic devices in HV ac substations, and many intelligent devices are still unable to operate reliably in the field even though they have passed the E-field compatibility standards. Some scholars have measured the transient voltage of ultrahigh voltage (UHV) gas insulated switch opening [8]. Literature [9] measured and suppressed the interference voltage at the smart device port when the switch is open. Literature [10] measured and analyzed the voltage coupled to the secondary cable from fast transient pulse disturbances. Literature [11] started research on sensors for transient electric field measurements with a view to capturing accurate electric field waveforms. All of the above studies have advanced the development of electromagnetic compatibility in substations, but because of the complex structure and coupling relationship

Manuscript received 3 January 2024; revised 6 April 2024; accepted 12 May 2024. Date of publication 16 May 2024; date of current version 4 September 2024. This work was supported in part by the National Natural Science Foundation of China under Grant 51877174 and Grant U1866201, in part by the State Grid Corporation Headquarters Science and Technology Project Fund Support under Grant 5226KY22000R, in part by the Technology Innovation Leading Program of Shaanxi under Grant 2024-QCY-KXJ-032, in part by the Natural Science Basic Research Key Project of Shaanxi under Grant 2024JC-ZDXM-31, and in part by the Doctoral Dissertation Innovation Fund of Xi'an University of Technology under Grant 252072301. Recommended for publication by Associate Editor Zheng Luo. *(Corresponding author: Jiandong Duan.)*

Wenchao Lu, Jiandong Duan, and Dongxing Dou are with the School of Electrical Engineering, Xi'an University of Technology, Xi'an 710048, China (e-mail: 1211911007@stu.xaut.edu.cn; duanjd@xaut.edu.cn; 2231921147@stu.xaut.edu.cn).

Lin Cheng and Jiangping Lu are with the Power Research Institute, State Grid Shaanxi Electric Power Company Ltd., Xi'an 710100, China (e-mail: chenglin@sn.sgcc.com.cn; lujiangping@sn.sgcc.com.cn).

Color versions of one or more figures in this article are available at https://doi.org/10.1109/TPEL.2024.3401706.

Digital Object Identifier 10.1109/TPEL.2024.3401706

of sensors, less consideration is currently given to observing the state of the disturbed equipment at the same time as the measurements are made, and then corresponding the measured physical quantities to the effects.

For complex interference assessment in actual conditions, it is difficult to accurately model the electrical structure and effect mechanism, and the propagation path of electromagnetic interference cannot be described quantitatively, which affects the reasonable assessment of key equipment. Probabilistic statistical methods were used to study the damage curve of different types of electronic devices (such as computer systems [12], [13], microprocessors and microcontrollers) under the threat of different electromagnetic environments, and compared the differences in the effect of different types of high-power electromagnetic pulse environments on devices and systems. Based on the physical mechanism, literature [14] extracted sensitive parameters as assessment indicators, and gave the basic steps for the electromagnetic vulnerability assessment. A method for risk assessment of systems using fuzzy mathematical theory was proposed [15].

Based on priori information, the existing assessment studies can be roughly divided into three categories [16]. For the first category, such as electric explosive devices, due to sufficient priori information, the entire action mechanism is clear and can be completely described by mathematical expressions [17]. Uncertain parameters of the model can be directly assessed by using different statistical methods and experimental data. Literature [18] proposed a multilevel vulnerability assessment model that reflects the mutual game between hidden variables. Literature [19] developed a multilevel vulnerability assessment model based on Bayesian methods under the condition of limited sample size. The second category can be represented by a hybrid model combining white box and black box, because only part of the vulnerable information is available. For example, combined Bayesian inference methods to quantify the specific failure process and put it into the model to solve with the assessment model [20]. The hybrid model of thermal process and hypothetical classifier was used to study the pulse breakdown characteristics of gas discharge tubes. For the third category, due to little understanding of the path and mechanism of interference, limited experimental data, and limited electric quantity that can be captured, a deterministic model cannot be established. Machine learning combining data-driven is a feasible choice. A nonparametric vulnerability assessment method is proposed in [21]. This method combines support vector machines and Gaussian process regression (GPR), in which only data is used to derive the final model without any prior model assumptions, achieving the purpose of assessment.

However, in many engineering application scenarios, there are still some situations that cannot be assessed. Due to limitations in measurement equipment or installation regulations, the data available is extremely limited (academically known as low measuring measurability [22]). This means that these data have become so scarce that even data-driven methods cannot be activated. Raissi et al. [23] proposed the physics-informed neural network (PINN) for the first time. The algorithm not only retains the advantages of data-driven machine learning algorithms, but also successfully adds prior knowledge such as physical laws to the modeling process of physical models. Unlike traditional regression, PINN requires only a small number of coordinate points to be entered, and the values of the desired variables are found through the constraints of partial differential equations, boundary conditions and initial conditions. PINN provides feasibility of effect assessment for low measuring testability limitation, which is focused on in this article. PINN has been demonstrated to be feasible for solving Wavefield Reconstruction Inversion and Maxwell's system of equations in several studies [24], [25]. In [26] and [27], PINN was used to solve the 1-D waveguide electromagnetic field problem for a given functional relationship. In [28], the 1-D time-varying electromagnetic field was solved for a given relation using PINN. Literature [29] explored performance of PINN in calculating 2-D magnetostatic case studies. However, the ability of PINN to solve 2-D EMI caused by transient interference sources remains to be investigated.

To solve the above problems, a multidimensional physical information electromagnetic interference assessment method based on PINN and GPR is proposed in this article. The research results are expected to provide reference for the assessment of interference effect of intelligent measurement devices under the limitation of measuring testability.

The core contributions of this article are as follows.

1) An optical current transformer (OCT) electromagnetic interference test is designed based on the actual engineering, and the voltage and magnetic field are measured.
2) For the first time, PINN was used to expand transient electromagnetic interference data in substation, and a radiation electric field training model was established using the partial differential equation of cable electromagnetic field. The radiation electric field data was obtained, taking into account both accuracy and speed.
3) Combined with the measured data and the calculated data, a 2-D GPR was used to establish a multi-input and multioutput electromagnetic interference effect assessment model, which can evaluate the probability of interference effect the disturbed equipment.

The rest of the article is organized as follows. Section II introduces the field situation and experimental design. Section III is the methodology of PINN and GPR. Section IV introduces the assessment model proposed in this article. Section V conducted a probability assessment of the effect of electromagnetic interference testing based on the proposed method. Finally, Section VI concludes this article.

II. Experimental and Variable Selection

The problems investigated in this article are as follows: In hierarchically connected UHV dc projects, the 1000 kV ac filter sub-bank in converter station is provided with two 500 kV circuit breakers. However, when the filter bank was put into operation and the circuit breaker was closed, the inconsistent OCT current at both ends frequently led to the differential protection misoperation. Even if no switching operation is performed, the alarm signal caused by the abnormal OCT signal often occurred in the

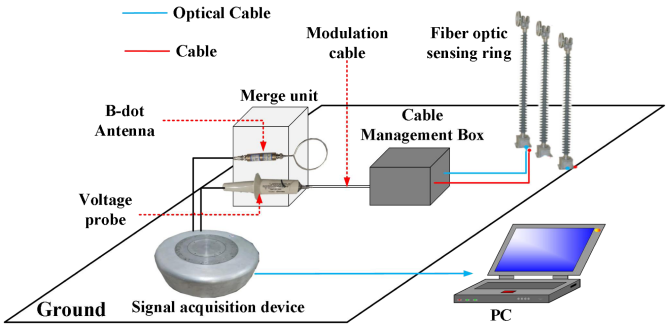

Fig. 1. Modulation cable interference monitoring test schematic diagram.

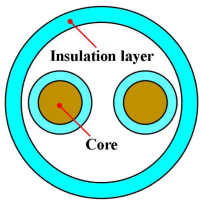

Fig. 2. Cross section of the modulation cable.

converter station. The field staff conducted output positioning on each electronic unit, basically excluding the fault of the primary equipment and electronic merging unit. After investigation, the fault was ultimately traced to the modulation cable between the outdoor cable management box (CMB) and the electronic unit.

Therefore, a 110-day electromagnetic signal monitoring testing in substation was conducted. As the substation is a running substation, according to the requirements of the operating organization, test cannot change the structure of a running OCT. A set of electromagnetic transient monitoring equipment was developed to capture as many electromagnetic interference signals as possible. Therefore, a set of electromagnetic transient monitoring equipment was developed to capture as many electromagnetic interference signals as possible. The available equipment in the substation includes voltage probes, current probes, magnetic field probes, and high-speed data acquisition cards. The voltage probe measures the voltage at the modulation cable port at merging unit (MU), while the magnetic field probe measures the spatial magnetic field of the modulation cable near MU. Due to the disability to destroy original wiring device of OCT, the current probe cannot be used. The high-speed acquisition card (placed in a cylindrical metal shielding tank) collects and outputs abnormal voltage and magnetic field signals, and simultaneously transmits them to the PC through optical fibers. For clarity, Fig. 1 is a test diagram.

The magnetic field near the cable port is measured using a B-dot small loop antenna, 0.4 m away from the vertical height of the cable. Modulation cable is a dual core unshielded cable.

During the monitoring period, 122 sets of transient signals were captured. Including 122 times disturbed, and 65 times alarms were caused by the abnormal amplitude of the modulation cable signal.

After investigation, the modulation cable actually used in the field is an unshielded dual-core cable LIY_0qmm75 [30], and the cable section is shown in Fig. 2. One of the dual-core cables is the working core with signal, and the other is the standby

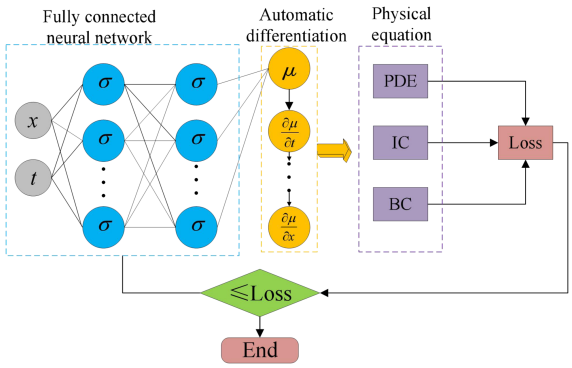

Fig. 3. Schematic diagram of PINN neural network structure.

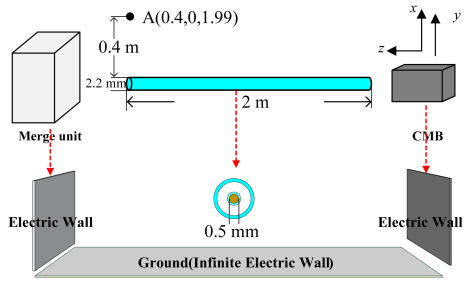

Fig. 4. Actual experimental equivalent model.

core. The cable size is 2 m × 2.2 mm. The inner core diameter is 0.5 mm.

Following the introduction of the test conditions, the article returns to the original goal of this article: to assess the risk of interference to equipment according to the actual electromagnetic environment. Under the premise of limited measurable variables, the electromagnetic environment at the measuring point is the dependent variable of the assessment object. The first step is to obtain the electromagnetic environment. After the magnetic field of the point is known, the electric field of the point needs to be calculated and assessed. The existing measurement data are only voltage and magnetic field, which are difficult to assess with the help of the existing cutting-edge inversion methods. Although the use of finite element simulation methods can be used to prediction to a certain extent, the test monitoring system is a complex structure with multiple conductors and multiple excitation. Even if the calculation can be performed, it is a time-consuming process. The requirements for the professional quality of the user are too high, and the engineering generalizability is weak. Moreover, there is a phenomenon of resource redundancy in the interference assessment under the condition of measuring testability limitation in this article. Therefore, the existing monitoring results of this test are considered to predict the electric field of the measurement position, and to provide auxiliary information for the assessment of electromagnetic interference effect, so as to improve the reliability of the assessment.

III. Methodology

A. Physics-Informed Neural Network (PINN)

Assume that the function $u = u(t, x)$ satisfies the following partial differential equation:

$$u_t + N(u, \lambda) = 0, x \in \Omega, t \in [0, T] \tag{1}$$

where, $N(\cdot)$ represents a differential operator, $N(u, \lambda)$ is a functional with parameter λ that differentiates u, x is a space variable, t is a time variable, u_t is the first-order partial derivative of u with respect to t, Ω is a subset of Euclidean space $\mathbb{R}^{\mathrm{D}}$, and T is the termination time.

Given the initial state, boundary conditions and physical parameter λ of $u(t, x)$, the traditional physical model can predict the value of $u(t, x)$ function at any point in space and time by solving the partial differential equation and using the obtained analytical solution. PINN considers establishing a neural network to approximate the solution of the partial differential equation. Define $u^{\mathrm{N}}(t, x)$ as the neural network that approximates the function $u(t, x)$, $r(t, x)$ as the residual of the partial differential equation, as shown in (2), and define the loss function Loss of PINN, as shown in the following:

$$r(t, x) = {u_t}^N + N\left(u^N, \lambda\right) \tag{2}$$

$$\mathrm{Loss} = \mathrm{Loss}_{\mathrm{init}} + \mathrm{Loss}_{\mathrm{bound}} + \mathrm{Loss}_{\mathrm{PDE}}. \tag{3}$$

Equation (4) and (5) are the data-driven part of the loss function, N_{init} and N_{bound} represent the initial conditions and boundary conditions calculated by data of samples, respectively. $\{{t^i}_{\mathrm{init}}, {x^i}_{\mathrm{init}}, u^i\}_{i=1}^{N_{\mathrm{init}}}$ and $\{{t^i}_{\mathrm{bound}}, {x^i}_{\mathrm{bound}}, u^i\}_{i=1}^{N_{\mathrm{bound}}}$ are the training data obtained according to the initial conditions and boundary conditions, which can also be obtained by experimental measurement or simulation generation

$$\mathrm{Loss}_{\mathrm{init}} = \frac{1}{N_{\mathrm{init}}} \sum_{i=1}^{N_{\mathrm{init}}} \left| u^N({t^i}_{\mathrm{init}}, {\mathrm{x}^i}_{\mathrm{init}}) - u^i \right|^2 \tag{4}$$

$$\mathrm{Loss}_{\mathrm{bound}} = \frac{1}{N_{\mathrm{bound}}} \sum_{i=1}^{N_{\mathrm{bound}}} \left| u^N({t^i}_{\mathrm{bound}}, {x^i}_{\mathrm{bound}}) - u^i \right|^2. \tag{5}$$

Equation (6) is the driving part of the physical model in the loss function, $\{{t^i}_{\mathrm{PDE}}, {x^i}_{\mathrm{PDE}}\}_{i=1}^{N_{\mathrm{PDE}}}$ is the training collocation point of the partial differential equation, and can be efficiently obtained by the automatic differentiation technique $r({t^i}_{\mathrm{PDE}}, {x^i}_{\mathrm{PDE}})$

$$\mathrm{Loss}_{\mathrm{PDE}} = \frac{1}{N_{\mathrm{PDE}}} \sum_{i=1}^{N_{\mathrm{PDE}}} \left| \mathrm{r}^N({t^i}_{\mathrm{PDE}}, {x^i}_{\mathrm{PDE}}) \right|^2. \tag{6}$$

When the value of the loss function reaches below the preset loss value, it not only indicates that the initial conditions and boundary conditions are close to being met, but also indicates that the data have met the constraint conditions defined by the partial differential equation. At this time, the trained neural network model is approximately equal to the function $u = u(t, x)$. The basic process of PINN is shown in Fig. 3.

B. Gaussian Process Regression (GPR)

According to the electromagnetic data calculation based on PINN in Section III-A, the numerical sequence of influencing factors of interference effect has been obtained. Measurements at the substation site can categorize the corresponding failure effects and assign them to indicators. According to the classification indicator of training data, GPR is suitable for regression, which can provide both mean and mean variance.

The GPR model is completely specified by its mean function and covariance function [31], which can be expressed as follows:

$$f(x) \sim GP(m(x), k(x, x')) \tag{7}$$

where $m(x)$ is the mean function; and $k(x, x')$ is the covariance function.

The mean function $m(x)$ represents the trend of the GPR model, which is usually defined as follows:

$$m(x) = g^T(x)\beta \tag{8}$$

where $g(x) = [g_1(x), g_2(x), \ldots, g_{\mathrm{n}}(x)]$ is the resistance vector, and β is the p-dimensional vector of the regression parameters.

The covariance function $k(x, x')$ models the dependence between two different values of the Gaussian process. In fact, the covariance function is the most important part of the Gaussian process regression, which controls the regularity of approximation. The selection of the kernel function requires that it satisfies Mercer's theorem, that is, any Gram matrix (kernel matrix) of the kernel function in the sample space is a semi-positive definite matrix. Their general expression can be described as follows:

$$k(x, x') = \sigma^2 r(x, x'; \theta) \tag{9}$$

where $\sigma^2$and θ are hyperparameters of the covariance function.

Squared exponential covariance function (SE covariance function) is

$$k(x, x') = \lambda_f^2 \exp\left(-\frac{1}{2}\frac{(x - x')}{\lambda_x^2}\right). \tag{10}$$

The training samples used for GPR learning are as follows:

$$\boldsymbol{X}^t = \left[x_1^t, x_2^t, \ldots, x_n^t\right] \tag{11}$$

$$\boldsymbol{C}^t = \left[c_1^t, c_2^t, \ldots, c_n^t\right]. \tag{12}$$

For Gaussian processes, in principle all samples obey the joint Gaussian distribution. Therefore, the prediction classification indicator at the predicted point $\boldsymbol{X}^p$ combined with the training data $\boldsymbol{X}^{\mathrm{t}}$ obeys the joint Gaussian distribution

$$\begin{pmatrix} f(\boldsymbol{X}^p) \\ f(\boldsymbol{X}^t) \end{pmatrix} \sim N\left(\begin{pmatrix} g(\boldsymbol{X}^p)\beta \\ \boldsymbol{G}\beta \end{pmatrix}, \sigma^2 \begin{pmatrix} 1 & r^T(\boldsymbol{X}^p) \\ r(\boldsymbol{X}^p) & \mathbf{R} \end{pmatrix}\right) \tag{13}$$

where $\mathbf{G} = g(\boldsymbol{X}^t)$ is the constructed matrix; $r(\boldsymbol{X}^p) = r(\boldsymbol{X}^p, \boldsymbol{X}^t; \theta)$ is the correlation vector between the predicted point and the training point; $\mathbf{R} = r(\boldsymbol{X}^t, \boldsymbol{X}^t; \theta)$ is the correlation matrix between the training points.

IV. Assessment Model of Electromagnetic Interference Effect

A. PINN Based Method for Predicting Electric Field Strength

In order to solve the electric field strength E_x of point A(0.4, 0, 1.99) at the end of the CMB cable, the field test problem is simplified as follows: when a voltage-conducting unshielded cable with a length of 2 m, an inner core diameter of 0.5 mm, and an outer diameter of 2.2 mm is placed on the earth's surface, the wave equation is used to calculate the near-field electric field in the x direction with a distance of 0.4 m from the end. Assuming that the cable extends along the z-axis direction. In the simulation calculation, the cable length is set to 2 m, respectively. The model is used to simulate the situation when the external cable is connected to the device, and the length of the external cable is 2 m, and only consider 1 single inner core connected to the circuit. The influence of the connector is also ignored here. For most connectors without filtering devices, this simplification is allowed. The simplified experimental equivalent model is shown in Fig. 4.

According to the problem description, the radius $r = 0.5$ mm is less than 0.4 m, so the partial differential equation is suitable for solving the near-field electric field intensity in this case. Assuming that the radius of the finite-length unshielded cylindrical cable is r, the length is L, the voltage is $V(t)$, the current is 0, and the transient magnetic field waveform at the end of the conductor is $H_y(t)$. The near-field electric field intensity $E_x(r, t)$ at A point should be solved, where r is the radial distance from the cable axis.

First, the partial differential equations of the electromagnetic field in the unshielded cable can be obtained, including Maxwell's equations and continuity equations as follows:

$$\begin{cases} \nabla \times \boldsymbol{E} = -\frac{\partial \boldsymbol{B}}{\partial t} \\ \nabla \times \boldsymbol{H} = \boldsymbol{J} + \frac{\partial \boldsymbol{D}}{\partial t} \\ \nabla \cdot \boldsymbol{B} = \boldsymbol{\rho} \\ \nabla \cdot \boldsymbol{D} = 0 \end{cases} \tag{14}$$

where $\boldsymbol{E}$ and $\boldsymbol{H}$ are the electric field and magnetic field intensity, $\boldsymbol{B}$ and $\boldsymbol{D}$ are the magnetic induction intensity and electric displacement vector, ρ is the charge density, and $\boldsymbol{J}$ is the current density.

For an unshielded cable of finite-length, determine the charge density and current density according to the geometry and current characteristics. Assuming that the cable is placed along the z-axis direction, the current density only has the z-direction component, namely. Assuming that the cable is a homogeneous medium and the charge density is 0, the continuity equation can be simplified as follows:

$$\nabla \cdot \boldsymbol{D} = \varepsilon_r \nabla \cdot \boldsymbol{E} = 0. \tag{15}$$

Then, the partial differential equation of the near-field electric field signal at point A need to be solved. The near-field electric and magnetic fields can be calculated by the first partial derivative of the electric field and magnetic field strengths

$$E_x = -\frac{\partial \phi}{\partial x} \tag{16}$$

$$H_{\mathrm{y}} = \frac{\partial A_z}{\partial x} - \frac{\partial A_x}{\partial z} \tag{17}$$

where φ is the electric potential function and A is the magnetic vector potential. Since the cable is unshielded and the magnetic field only surrounds the cable in one loop, we can assume that $A_y = 0$. At the same time, since the cable is a straight line, φ and A is only related to x. Therefore, we can obtain the partial differential equation of the near-field electric field signal

$$\frac{\partial^2 E_x}{\partial x^2} = \mu_0 \varepsilon_r \frac{\partial^2 E_x}{\partial t^2} - \mu_0 \frac{\partial^2 H_y}{\partial t^2} \tag{18}$$

where μ_0 is the magnetic permeability in vacuum, and ε_{r} is the dielectric constant of air.

Due to the fact that the subscripts x and y in E_x and H_y represent the electric and magnetic field strengths in the x and y directions of the coordinate axes, in order to avoid confusion in reading, using E and H instead of E_x and H_y in the following text.

Finally, it should be noted that, since the cable is finite in length, boundary conditions need to be considered in actual calculations. At the end of the cable, the cut-off of current and potential should be considered, namely $I(t) = 0$, $\varphi(0.4, 0, 1.99) = 0$. This is a boundary condition in fact.

Known through Section III-A, the PINN solution requires a preset initial conditions, boundary conditions and partial differential equation (PDE) conditions.

The initial condition (IC) is the true solution at time $t = 0$, including the position and the preset initial conditions. In this problem, the initial function can be written as follows:

$$\mathrm{IC}: \begin{cases} E_i^{\mathrm{T}}(t=0) \\ H_i^{\mathrm{T}}(t=0) \end{cases} (i = 1, 2, 3 \ldots N_0) \tag{19}$$

where i represents the sampling point, N_0 represents the number of sampling points for the initial condition, ${E_i}^{\mathrm{T}}$ and ${H_i}^{\mathrm{T}}$ are the initial input magnetic and electric field data, respectively.

The boundary condition (BC) including the position of the boundary point and the preset boundary conditions. In this article, the ideal conductor boundary conditions are used, where the electric field intensity is equal to zero at the boundary, and the first partial derivative of the magnetic field intensity is equal to zero at the boundary. The setting of the boundary condition function is shown in the following:

$$\mathrm{BC}: \begin{cases} E_i^{\mathrm{P}}(x=0) = 0 \\ \nabla \times H_i^{\mathrm{P}}(x=0, x= \\ \quad 0.5, z=0, z=2) = 0 \end{cases} (i = 1, 2, 3 \ldots N_b) \tag{20}$$

where N_{b} represents the number of sampling points of the boundary condition, and ${E_i}^{\mathrm{P}}$ and ${H_i}^{\mathrm{P}}$ are boundary magnetic and electric field data, respectively.

The PDE loss function is generated by the preset PDE system. This function measures the residual error of the predicted solution in the PDE system, that is, the degree to which the solution satisfies the system. According to (18), the physical partial differential equation constraint of the PINN based on the

Maxwell equations is as follows:

$$\text{PDE}: \frac{\partial^2 E_{\text{i}}}{\partial x^2} - \mu_0 \varepsilon_r \frac{\partial^2 E_i}{\partial t^2} + \mu_0 \frac{\partial^2 H_i}{\partial t^2} (i = 1, 2, 3 \ldots N_{\text{PDE}}) \tag{21}$$

where N_{PDE} represents the number of sampling points in the computing domain, μ_0 is the magnetic permeability in vacuum, and ε_{r} is the dielectric constant of air.

With the above BC, IC, and PDE conditions it is possible to construct the corresponding loss function and thus perform the PINN solution. The goal of optimizing the loss function is to minimize the value of the loss function, so that the solution generated by the neural network satisfies the PDE system and the preset physical conditions. The loss function of PINN is the mean square error (MSE) of the resulting single equation, shown in the following:

$$\text{Loss} = \text{MSE}_{\text{PDE}} + \text{MSE}_{\text{IC}} + \text{MSE}_{\text{BC}}. \tag{22}$$

PDE loss function is shown as follows:

$$\text{MSE}_{\text{PDE}} = \text{Loss}_{\text{PDE}} = \frac{1}{N_{\text{PDE}} \times N_{\text{PDE}}} \sum_{i=1}^{N_{\text{PDE}} \times N_{\text{PDE}}} |g_i|^2 \tag{23}$$

$$g = \frac{\partial^2 E}{\partial x^2} - \mu_0 \varepsilon_r \frac{\partial^2 E}{\partial t^2} + \mu_0 \frac{\partial^2 H}{\partial t^2} \tag{24}$$

where N_{PDE} represents the number of sampling points in the computing domain.

Initial conditional loss function is shown as follows:

$$\text{MSE}_{\text{IC}} = \text{Loss}_{\text{IC}} = \frac{1}{N_0 \times N_0} \sum_{i=1}^{N_0 \times N_0} \left(\left| E_i^{\text{P}} - E_i^{\text{T}} \right|^2 + \left| H_i^{\text{P}} - H_i^{\text{T}} \right|^2 \right) \tag{25}$$

where i represents the sampling point, N_0 represents the number of sampling points for the initial condition, ${E_i}^{\text{T}}$ and ${H_i}^{\text{T}}$ are the initial input magnetic and electric field data, respectively, and ${E_i}^{\text{P}}$ and ${H_i}^{\text{P}}$ are initial magnetic and electric field data, respectively.

In this article, the initial conditions are the electric and magnetic field strength data at $t = 0$. The voltage data were measured. Based on the principle of radiation and mathematical modelling of a finite length straight conductor [32], the initial electric and magnetic field strengths E^{T} and H^{T} can be determined as shown in the following:

$$E^{\text{T}} = \frac{Z_0 I_0 l}{2\lambda x} \sqrt{1 - \left(\frac{\lambda}{2\pi x} \right)^2 + \left(\frac{\lambda}{2\pi x} \right)^4} \tag{26}$$

$$H^{\text{T}} = \frac{I_0 l}{2\lambda x} \sqrt{1 + \left(\frac{\lambda}{2\pi x} \right)^2} \tag{27}$$

where I_0 is the current value at the initial moment $t = 0$, due to the conductor is extremely short, the resistive characteristics of the obvious, the size of the approximation to take 0.01 times the voltage; l is the length of the conductor; λ is the wavelength; x is the target point and the conductor perpendicular distance (this article seeks to take the range of 0–0.5 m); Z_0 is the free-space wave impedance, take 120π.

Boundary condition loss function measures the error between the predicted solution of the neural network and the true solution at the boundary, as follows:

$$\text{MSE}_{\text{BC}} = \text{Loss}_{\text{BC}} = \frac{1}{N_b} \sum_{i=1}^{N_b} \left(\left| E_i^P \right|^2 + \left| \nabla \times H_i^P \right|^2 \right) \tag{28}$$

where N_{b} represents the number of sampling points of the boundary condition, and E^P and H^P are both boundary point magnetic and electric field data, respectively.

The minimization of ($\text{Loss}_{\text{BC}} \to 0$) and ($\text{Loss}_{\text{IC}} \to 0$) enforces the BC and IC at a set of finite sampling points on the boundary surfaces and at the initial state. In addition, actual measured magnetic field strength data for a single point [at position ($x = 0.4$, $z = 1.99$) in the $x0z$ coordinate system] should also be included.

B. Multidimensional Gaussian Process

GPR is usually a single input single output model. In this application, if need to study the electromagnetic interference effect under the joint action of magnetic field and electric field and other multidimensional parameters, the GPR model under multiple inputs should be considered. Often use vector representation to write multiple input functions, such as $f(x)$, where x is an input vector of size n. Note that subscripts have been used to distinguish different input points $x_1, x_2, \ldots, x_{\text{n}}$, thus using superscripts to distinguish different elements within the same input point x. The covariance function adopts the square exponential function, and the squared exponential covariance function is now given by the following [33]:

$$k(x, x') = \lambda_f^2 \exp\left(-\frac{1}{2} (x - x')^T \Lambda_x^{-1} (x - x') \right). \tag{29}$$

The parameter λ_f is the same as before, but the matrix Λx is new. It is the matrix of squared length scales for the input. In practice, assume it to be a diagonal matrix

$$\Lambda_x = \begin{bmatrix} \lambda_{x1}^2 & \cdots & 0 \\ \vdots & \ddots & \vdots \\ 0 & \cdots & \lambda_{xm}^2 \end{bmatrix}. \tag{30}$$

The quantities $\lambda_{x1}, \ldots, \lambda_{xm}$ effectively determine how much the Gaussian process can vary when the corresponding input parameters $x1, x2 \ldots, xm$ vary.

Combined with (13), the regression obtained by GPR is shown as follows:

$$\hat{m}(\boldsymbol{X}^p) = g(\boldsymbol{X}^p)\beta + r^T(\boldsymbol{X}^p)\mathbf{R}^{-1}(C^t - \boldsymbol{G}\beta) \tag{31}$$

$$\hat{s}^2(\boldsymbol{X}^p) = \sigma^2(1 - r^T(\boldsymbol{X}^p)\mathbf{R}^{-1}r(\boldsymbol{X}^p)) \tag{32}$$

where $\mathbf{G}$ is the constructed matrix; $r(\boldsymbol{X}^p) = r(\boldsymbol{X}^p, \boldsymbol{X}^t; \theta)$ is the correlation vector between the predicted point and the training point; and $\mathbf{R} = r(\boldsymbol{X}^t, \boldsymbol{X}^t; \theta)$ is the correlation matrix between the training points.

C. Calculation of Multistate Probability

The output E of the PINN in Section IV-A is maximized to obtain $E_{\max}$, and the corresponding measured $H_{\max}$ is also input to the 2D-GPR in Section IV-B together. And the evaluation indicators in different states are obtained, and the calculation of the failure probability in different states can be carried out next. Multidimensional GPR can get regression under different effect. Assuming that the equipment to be assessed has m failure states, the classification indicator of each state is assessed, and the assessed distribution of each state i on each point x^p can be expressed as follows:

$$C_i^p = f_i(c|x^p) \sim N\left(\mu_i^p, \sigma_i^p\right) \quad i = 1, 2, \ldots, m \tag{33}$$

where μ and σ come from the output distribution results of the GPR.

Based on the assumption that the point belongs to the state with the largest classification indicator, the probability of state k can be calculated as (34). In this way, the probability of each state in the predicted point can be calculated

$$\begin{aligned} P_k^p &= P(C_k^p = \max(C_0^p, C_1^p, \ldots, C_m^p)) \\ &= P\left(C_k^p \geq C_0^p, \ldots, C_k^p \geq C_{k-1}^p, C_k^p \right. \\ &\quad \left. \geq C_{k+1}^p, \ldots, C_k^p \geq C_m^p\right) \\ &= \int_{-\infty}^{+\infty} f_k(c|x^p) \cdot \left(\int_{-\infty}^{c} f_0(c|x^p)dc \cdots \int_{-\infty}^{c} f_{k-1}(c|x^p)dc \right. \\ &\quad \left. \int_{-\infty}^{c} f_{k+1}(c|x^p)dc \cdots \int_{-\infty}^{c} f_m(c|x^p)dc \right). \end{aligned} \tag{34}$$

Taking this test as an example, the electromagnetic interference effect is denoted as no interference (state 0) and disturbance interference (state 1). Therefore, the probability distribution of the equipment in state 0 and 1 after suffering electromagnetic interference is shown in the following:

$$\begin{aligned} P_1^p &= P(C_1^p = \max(C_0^p, C_1^p)) \\ &= \int_{-\infty}^{+\infty} f_1(1|x^p) \cdot \left(\int_{-\infty}^{1} f_0(1|x^p)dc \right) dc \end{aligned} \tag{35}$$

$$\begin{aligned} P_0^p &= P(C_0^p = \max(C_0^p, C_1^p)) \\ &= \int_{-\infty}^{+\infty} f_0(0|x^p) \cdot \left(\int_{-\infty}^{0} f_1(0|x^p)dc \right) dc. \end{aligned} \tag{36}$$

The overall process of the assessment method proposed in this article is shown in Fig. 5.

The whole process can be divided into the following steps.

Step 1: A total of N sets of measurement data. Import the n_{th} ($n = 1,2,3 \ldots N$)measured H data, BC and IC data matrices into the PINN network.

Step 2: According to the preset partial differential equations, the PINN network starts to train with the loss function (22) as the objective until the convergence condition is satisfied.

Step 3: The PINN network training is completed and the evaluated E_n data is obtained.

Step 4: The n_{th} ($H_{\max}$, $E_{\max}$) is recorded based on the corresponding measured H data and evaluated E data. Let $n = n + 1$, proceed to Step 1. When $n = N$, proceed to Step 5.

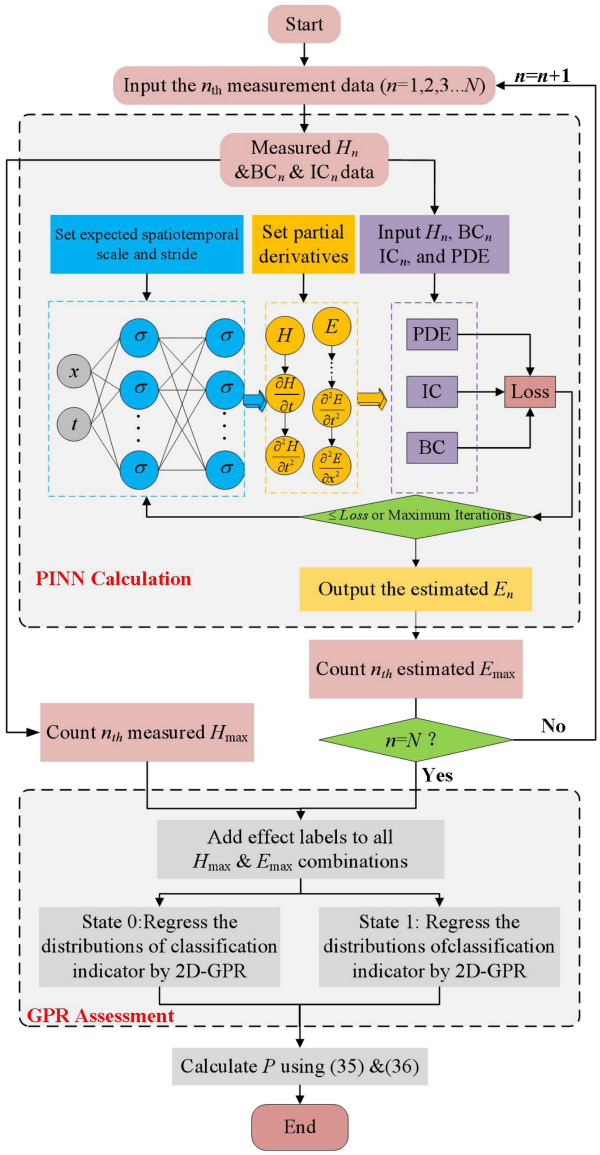

Fig. 5. Overall flowchart of the method in this article.

Step 5: Mark the N groups of data with 0 or 1 effect according to the substation field effect observation results.

Step 6: Use 2D-GPR for effect regression assessment indicator calculation.

Step 7: Calculate the probability distributions under different effects by evaluating the indicators using (35) and (36).

V. Case Study

A. Electric Field Strength Calculation

Fig. 6 shows the modulation cable measurement platform. The magnetic field antenna is a self-developed B-dot antenna, with a calculated 3 dB transition frequency of 106.26 MHz. The signal acquisition equipment uses the PicoScope 5402 oscilloscope. The maximum measurement bandwidth can reach 200 MHz and the sampling rate is 1 GS/s The modulation cable connects the cable management box and merging unit.

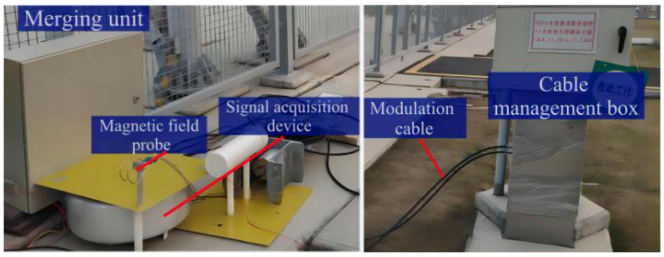

Fig. 6. Modulation cable measurement platform.

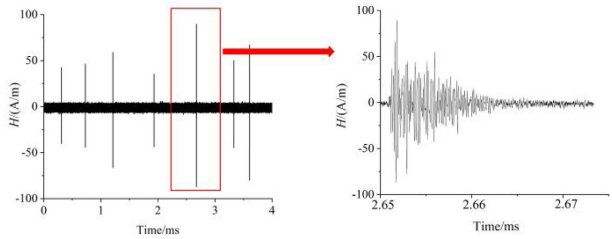

Fig. 7. Radiated magnetic field waveform (macro-waveform and micro-waveform).

The macropulse waveform of the magnetic field intensity obtained by the test is shown in Fig. 7.

The left figure of Fig. 7 is the macro waveform of the radiation magnetic field recorded in the substation test. As shown in Fig. 7, the "vertical line" of the macro waveform represents the magnetic field jump of each transient interference, and the transient interference process begins from here. With the disappearance of the attenuation oscillation process, the transient process ends, and the next interference is waiting. The details of the macro waveform (the part in the red box) are extended, which are similar to the damped oscillation pulses. This process is repeated until the end of the disturbance. At the same time, each transient pulse can be considered to be caused by the transient voltage and current on the conductor.

When selecting magnetic field data H used in PINN every time, the transient pulse with the highest peak in the macro waveform is selected. Select 201 data points near the highest peak as inputs ($\mathbf{H}(x = 0.4, z = 1.99)$) and use its corresponding 201 voltage data points to calculate the initial electric ($\mathbf{E}(t = 0)$) and magnetic field ($\mathbf{H}(t = 0)$) data (length of 2 μs at 100 MHz sampling frequency).

The dataset before each PINN solution in this article include the following data (shown in Fig. 8)

1) Boundary condition data BC: Let boundary electric field data $\mathbf{E}(x = 0) = 0$ (one 201 $\times$ 1 matrix), boundary magnetic field data $\frac{\partial \mathbf{H}}{\partial x}(x = 0 \& x = 0.5 \& y = 0 \& y = 2)$ (Four 201 $\times$ 1 matrices).
2) Initial condition data IC: Initial electric field data $\mathbf{E}(t = 0)$ (one 201 $\times$ 201 matrix), initial magnetic field data $\mathbf{H}(t = 0)$ (one 201 $\times$ 201 matrix).
3) Magnetic field strength data at the actual measurement point ($x = 0.4$, $z = 1.99$) (one 201 $\times$ 1 matrix).

Set the training step size to be 3000 steps and the convergence error to be 10^{-4} [34], [27], and the once loss profile obtained is shown in Fig. 9.

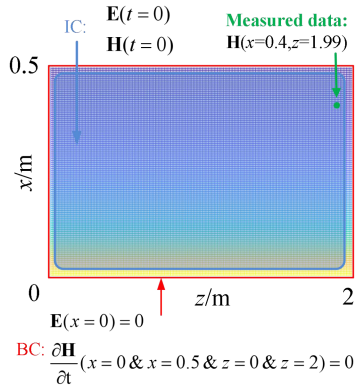

Fig. 8. Input data used in the PINN.

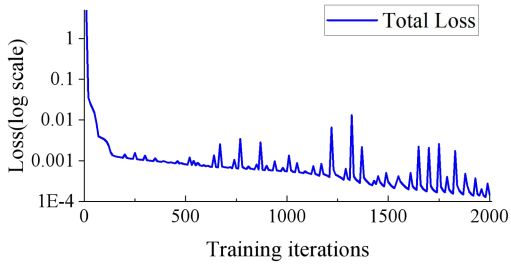

Fig. 9. Loss curves of training.

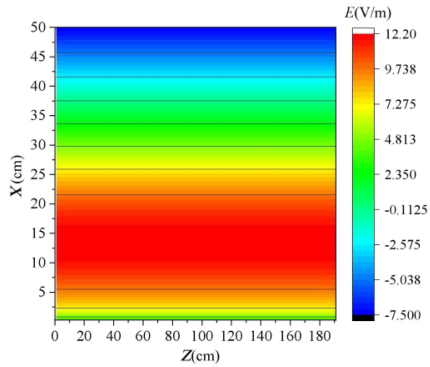

Fig. 10. Electric field distribution waveform predicted by PINN ($t = 0.2$ μs).

Fig. 10 shows the 2-D electric field distribution at the $x0z$ plane calculated by PINN ($t = 0.2$ μs), The electric field amplitude of point A can be obtained directly. A total of 122 sets of data were calculated.

To verify the effectiveness of PINN prediction. According to the 122 groups of measured voltage data at the test site, the 3-D electromagnetic field simulation is carried out by using the finite integral time-domain method to monitor the electric field strength of the target point A (see Fig. 11). The peak value of each group of simulation calculation data is compared with the peak value of the electric field strength predicted by PINN, and the correlation distribution diagram is obtained as shown in Figs. 12 and 13. It can be seen that the prediction result by PINN method in this article has strong equivalence.

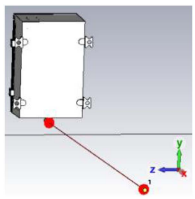

Fig. 11. Calculation model of time-domain finite integral method.

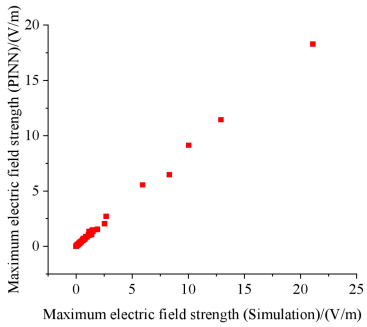

Fig. 12. Comparison of electric field intensity amplitude distribution.

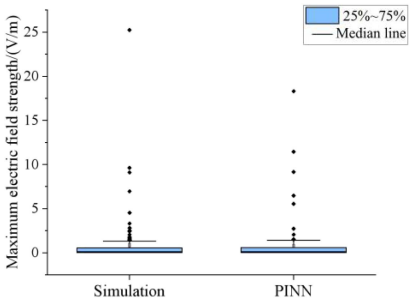

Fig. 13. Boxplot of electric field intensity amplitude distribution.

B. Interference Effect Probability Assessment

The PINN prediction and subsequent assessment in this article are based on the following important conditions: 1) the electromagnetic field at the location of concern belongs to the near field electromagnetic field, and the electric field in the near field is mainly related to voltage, and the magnetic field is mainly related to current; 2) the transient pulse occurrence time of current and voltage is highly consistent, which also leads to the well one-to-one correspondence between the single pulse disturbance time and peak value of the transient electric field and magnetic field. It can be expressed as follows:

$$\boldsymbol{H} \propto I \tag{37}$$

$$\boldsymbol{E} \propto U. \tag{38}$$

Based on the above conditions, do not need to pay attention to the full waveform of magnetic field and electric field of each "interference event." The effect can be assessed only by using the amplitude data of the predicted electric field and the measured magnetic field, plus their corresponding interference effect.

Thus, the failure assessment criterion is whether the OCT sends an alarm during the actual field test. If no alarm is sent, it is normal state and is denoted as state 0. If an alarm is sent, it is abnormal state and is denoted as state 1. The corresponding states under the measured magnetic field amplitude and the predicted electric field amplitude are shown in Fig. 14. 122 sets of tests include 65 sets of state 1 (Red) and 57 sets of state 0 (Blue).

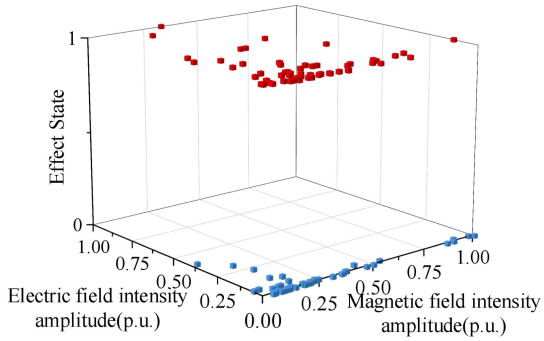

Fig. 14. Experimental results of two states under electromagnetic interference.

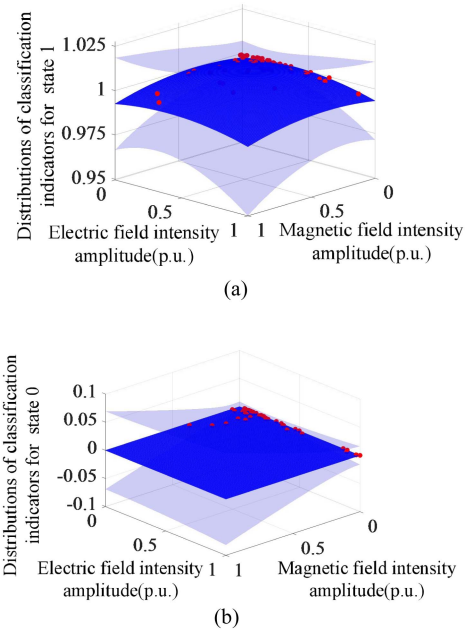

Fig. 15. Distributions of classification indicators for each state of OCT. (a) State 1. (b) State 0.

Since there are two states in this case, in the GPR assessment part, the square exponential kernel function is used for both states. The distributions of classification indicators for each state are shown in Fig. 15.

Finally, by comparing the distributions of the classification indicators of each state, the probability assessment results based on (35) and (36) can be calculated. As shown in Fig. 16.

Similarly, according to the complexity theory of electromagnetic environment, the complexity of electric field signal and magnetic field signal can be calculated. The traditional complexity C_{OC} is calculated by (39) [35]. The "two input-two output" assessment model is established based on the input of complexity and the output of assessment effect. The obtained assessment probability diagram is shown in Fig. 17.

$$C_{\mathrm{OC}} = T_{\mathrm{P}} \times F_{\mathrm{P}} \times E_{\mathrm{P}} \tag{39}$$

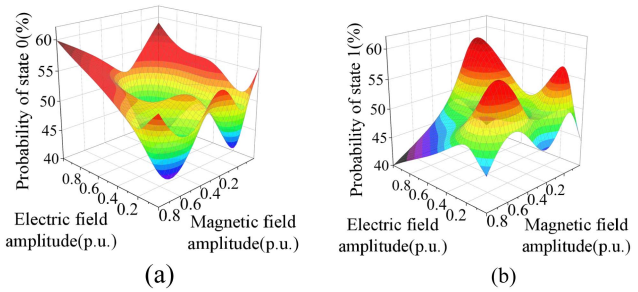

Fig. 16. Interference effect probability distribution based on electric field and magnetic field strength. (a) State 0. (b) State 1.

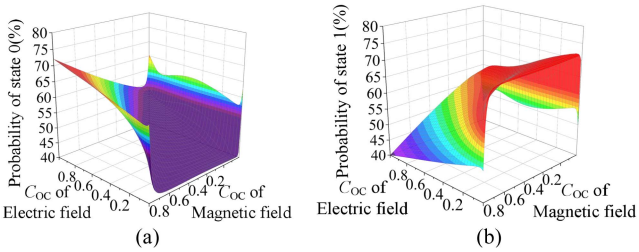

Fig. 17. Interference effect probability distribution based on the traditional complexity of electric field and magnetic field. (a) State 0. (b) State 1.

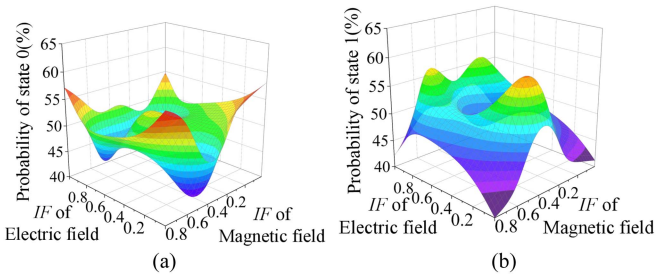

Fig. 18. Interference effect probability distribution based on the objective complexity of electric field and magnetic field. (a) State 0. (b) State 1.

where T_{P} represents the time domain occupancy of the signal, F_{P} represents the frequency domain occupancy of the signal, E_{P} represents the energy occupancy of the signal.

In this article, a complexity assessment indicator based on time spectrum characteristic frequency is proposed as shown in the following:

$$\mathrm{IF} = \frac{\max[(|S(t,f)| - S_0)]}{\mathrm{e}^{\left|f_{\max[S(t,f)]} - f_{\mathrm{sub}}\right|} \times R_\alpha} \tag{40}$$

where $f_{\max[|S(\tau,f)|]}$is the frequency point corresponding to the maximum time-frequency distribution intensity of the interference signal, f_{sub} is the characteristic frequency of the subjectively determined sensitive equipment, 15 MHz here. R_α is the Rényi entropy [20], and it represents the time-frequency aggregation of the electromagnetic interference signal.

As shown in Figs. 17 and 18, electromagnetic complexity can also assess the effect probability under given electromagnetic conditions. And the complexity assessment indicator proposed in this article also presents a multiple peak valley result similar to Fig. 14, which has certain reference value for the assessment EMI of radiation environment.

VI. Conclusion

Aiming at the effect assessment problem of electrical power measurement equipment under various interference, a multidimensional failure assessment method is proposed under the condition of measuring testability limitation. The method combines PINN and GPR, in which data are used to infer, and the final model does not have any priori model assumptions. First, the electric field data are predicted by combining electromagnetic theory and PINN, and the classification indicator is constructed according to the actual effect. Then, the classification indicators of the predicted area are averaged and confidence interval regressions are carried out by GPR. Through multidimensional GPR, the probability of multiple effect states can be assessed at the same time.

In order to illustrate the applicability and effectiveness of this method, a group of tests are carried out on a system of OCT equipment under the radiation environment with measuring testability limitation, and the case is studied from different perspectives. In further research, it is of importance to study the accuracy of the assessment results, and faster calculation of necessary changes in the case under measuring testability limitation.

References

[1] T. Peikert, H. Garbe, and S. Potthast, "Fuzzy-based risk analysis for IT-systems and their infrastructure," *IEEE Trans. Electromagn. Compat.*, vol. 59, no. 4, pp. 1294–1301, Aug. 2017.

[2] C. Schwabe, N. Thönelt, J. Lutz, and T. Basler, "High cycle fatigue testing of silicon IGBT devices under application-close conditions," *IEEE Trans. Power Electron.*, vol. 38, no. 11, pp. 14516–14525, Nov. 2023.

[3] J. Yao, S. Wang, and Z. Luo, "Modeling, analysis, and reduction of radiated emi due to the voltage across input and output cables in an automotive non-isolated power converter," *IEEE Trans. Power Electron.*, vol. 37, no. 5, pp. 5455–5465, May 2022.

[4] W. H. Siew, Q. Li, M. G. Stewart, K. Walker, and C. Piner, "Measurement of electromagnetic emissions from FACTS equipment operational within substations - part I," *IEEE Trans. Power Del.*, vol. 20, no. 2, pp. 1775–1181, Apr. 2005.

[5] J. Zhang, T. Lu, W. Zhang, X. Bian, and X. Cui, "Characteristics and influence factors of radiated disturbance induced by IGBT switching," *IEEE Trans. Power Electron.*, vol. 34, no. 12, pp. 11833–11842, Dec. 2019.

[6] J. Fan et al., "Electromagnetic disturbance characteristics and influence factors of PETT oscillation in high-voltage IGBT devices," *IEEE Trans. Power Electron.*, vol. 36, no. 4, pp. 4116–4124, Apr. 2021.

[7] X. Kong et al., "Noninvasive and accurate measuring method of the MMC and HVDC circuit breaker action moment based on transient E-field pulse," *IEEE Trans. Power Electron.*, vol. 37, no. 11, pp. 13332–13342, Nov. 2022.

[8] Y. Gongchang, L. Weidong, C. Weijiang, G. Yonggang, and L. Zhibing, "Development of full frequency bandwidth measurement of VFTO in UHV GIS," *IEEE Trans. Power Del.*, vol. 28, no. 4, pp. 2550–2557, Oct. 2013.

[9] H. Wu, C. Jiao, and X. Cui, "Study on coupling of very fast transients to secondary cable via a test platform," *IEEE Trans. Electromagn. Compat.*, vol. 60, no. 5, pp. 1366–1375, Oct. 2018.

[10] S. Ge, W. Liu, X. Li, and D. Ding, "Coupling characteristics of electromagnetic disturbance of on-site electronic device power port in substations and its suppression," *IEEE Trans. Electromagn. Compat.*, vol. 63, no. 5, pp. 1584–1592, Oct. 2021.

[11] X. Ni, P. Qiu, B. Zhang, Y. Song, L. Song, and S. He, "Design of nanosecond-level transient electric field sensor and its application in HVDC converter station," in *Proc. IEEE 7th Glob. Electromagn. Compat. Conf.*, 2023, pp. 66–67.

[12] A. Vaccaro and P. Magnone, "Influence of power cycling test methodology on the applicability of the linear damage accumulation rule for the lifetime estimation in power devices," *IEEE Trans. Power Electron.*, vol. 38, no. 5, pp. 6545–6554, May 2023.

[13] M. Camp and H. Garbe, "Susceptibility of personal computer systems to fast transient electromagnetic pulses," *IEEE Trans. Electromagn. Compat.*, vol. 48, no. 4, pp. 829–834, Nov. 2006.
[14] V. Chepelev et al., "Methodical approach for immunity assessment of electronic devices excited by high power EMP," *J. Electron. Testing*, vol. 34, no. 5, pp. 547–557, Sep. 2018.
[15] G. Zeng, C. Herold, T. Methfessel, M. Schäfer, O. Schilling, and J. Lutz, "Experimental investigation of linear cumulative damage theory with power cycling test," *IEEE Trans. Power Electron.*, vol. 34, no. 5, pp. 4722–4728, May 2019.
[16] Y. Chen, K. Li, Z. Wang, Y. Zhou, and Y. Xie, "Vulnerability assessment method for electronic devices excited by transient electromagnetic disturbances," *IEEE Electromagn. Compat. Mag.*, vol. 11, no. 4, pp. 94–99, Oct.–Dec. 2022.
[17] J. J. Pantoja, N. Pena, F. Rachidi, F. Vega, and F. Roman, "Characterization, modeling, and statistical analysis of the electromagnetic response of inert improvised explosive devices," *IEEE Trans. Electromagn. Compat.*, vol. 56, no. 2, pp. 393–403, Apr. 2014.
[18] K.-J. Li, Y.-Z. Xie, Y.-H. Chen, and Y.-C. Hui, "Multinomial regression model for the assessment of multilevel effects caused by high-power electromagnetic environments," *IEEE Trans. Electromagn. Compat.*, vol. 61, no. 1, pp. 149–156, Feb. 2019.
[19] Y. Liu, F. Han, J. Wang, and H. Qi, "Vulnerability assessment of a multistate component for IEMI based on a bayesian method," *IEEE Trans. Electromagn. Compat.*, vol. 61, no. 2, pp. 467–475, Apr. 2019.
[20] K.-J. Li, Y.-Z. Xie, Y.-H. Chen, Y. Zhou, and Y.-C. Hui, "Bayesian inference for susceptibility of electronics to transient electromagnetic disturbances with failure mechanism consideration," *IEEE Trans. Electromagn. Compat.*, vol. 62, no. 5, pp. 16690–11677, Oct. 2020.
[21] Y.-H. Chen et al., "Vulnerability assessment of equipment excited by disturbances based on support vector machine and Gaussian process regression," *IEEE Trans. Electromagn. Compat.*, vol. 63, no. 1, pp. 103–110, Feb. 2021.
[22] L. Chen, J. Liu, Z. Zhang, and Z. Pan, "Analysis and application on engineering testability of parameter estimation in power system based on Monte Carlo method," *CSEE J. Power Energy Syst.*, to be published, doi: 10.17775/CSEEJPES.2022.03720.
[23] M. Raissi, P. Perdikaris, and G E. Karniadakis, "Physics-informed neural networks: A deep learning framework for solving forward and inverse problems involving nonlinear partial differential equations," *J. Comput. Phys.*, vol. 378, pp. 686–707, Feb. 2019.
[24] C. Song and T. A. Alkhalifah, "Wavefield reconstruction inversion via physics-informed neural networks," *IEEE Trans. Geosci. Remote Sens.*, vol. 60, 2022, Art. no. 5908012.
[25] M. Baldan, P. Di Barba, and D. A. Lowther, "Physics-informed neural networks for inverse electromagnetic problems," *IEEE Trans. Magn.*, vol. 59, no. 5, May 2023, Art. no. 7001705.
[26] P. Zhang, Y. Hu, Y. Jin, S. Deng, X. Wu, and J. Chen, "A maxwell's equations based deep learning method for time domain electromagnetic simulations," *IEEE J. Multiscale Multiphys. Comput. Techn.*, vol. 6, pp. 35–40, 2021.
[27] P. Zhang, Y. Hu, Y. Jin, S. Deng, X. Wu, and J. Chen, "A maxwell's equations based deep learning method for time domain electromagnetic simulations," in *Proc. IEEE Texas Symp. Wireless Microw. Circuits Syst.*, 2020, pp. 1–4.
[28] G. Baldan, M. Baldan, and B. Nacke, "Solving 1D non-linear magneto quasi-static Maxwell's equations using neural networks," *Int. Eng. Technol. Sci. Meas. Technol.*, vol. 15, no. 2, pp. 204–217, Mar. 2021.
[29] Z. Gong, Y. Chu, and S. Yang, "Physics-informed neural networks for solving 2-D magnetostatic fields," *IEEE Trans. Magn.*, vol. 59, no. 11, Nov. 2023, Art. no. 7002005.
[30] Y. Guo, K. Hong, W. Xu, F. Li, and X. Chen, "Simulation and analysis of the influence of external cables on the electromagnetic radiation of the electronic equipment," in *Proc. IEEE MTT-S Int. Conf. Numer. Electromagn. Multiphys. Model. Optim.*, 2020, pp. 1–4.
[31] J. P. Jacobs, S. Koziel, and S. Ogurtsov, "Computationally efficient multifidelity bayesian support vector regression modeling of planar antenna input characteristics," *IEEE Trans. Antennas Propag.*, vol. 61, no. 2, pp. 980–984, Feb. 2013.
[32] Z. Yang, Y. Liu, G. Zhou, X. Lin, T. Ji, and B. Li, "Method of mechanical fault intelligent diagnosis based on vibration signal of high voltage circuit breaker," *High Voltage App.*, vol. 50, no. 4, pp. 1–6, Jul. 2014.
[33] B. Yin, C. Chen, L. Zuo, B. Li, L. Yuan, and Y. He, "An assessment method of electromagnetic interference based on a fast s-transform and time-frequency space model," *IEEE Trans. Electromagn. Compat.*, vol. 64, no. 2, pp. 396–404, Apr. 2022.
[34] S. Li, Z. Liu, S. Fu, Y. Wang, and F. Xu, "Intelligent beamforming via physics-inspired neural networks on programmable metasurface," *IEEE Trans. Antennas Propag.*, vol. 70, no. 6, pp. 4589–4599, Jun. 2022.
[35] R. G. Baraniuk, P. Flandrin, A. J. E. M. Janssen, and O. J. J. Michel, "Measuring time-frequency information content using the Renyi entropies," *IEEE Trans. Inf. Theory*, vol. 47, no. 4, pp. 1391–1409, May 2001.

Wenchao Lu (Student Member, IEEE) was born in Hanzhong, China, in 1995. He received the bachelor's degree in electrical engineering from Southwest Jiaotong University, Chengdu, China, in 2018, and the master's degree in electrical engineering in 2021 from the Xi'an University of Technology, Xi'an, China, where he is currently working toward the doctoral degree in electrical engineering.

His research interests include electromagnetic interference and relay protection of equipment.

Jiandong Duan (Member, IEEE) received the B.S. degree from the Huazhong University of Science and Technology, Hubei, China, in 1995, the M.S. degree from Guangxi University, Nanning, China, in 1998, and the Ph.D. degree from Xi'an Jiaotong University, Xi'an, China, in 2005, all in electrical engineering.

He is currently a Professor with the School of Electrical Engineering, Xi'an University of Technology. His research interests include power system analysis, dc distribution networks, distributed multienergy system, relay protection, and smart grid monitoring technology.

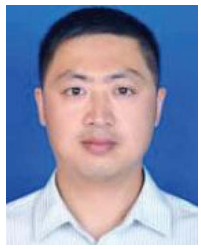

Lin Cheng received the Ph.D. degree in electrical engineering from Xi'an Jiaotong University, Xi'an, China, in 2012.

He is currently working with the Power Research Institute, State Grid Shaanxi Electric Power Company Limited, Xi'an. His main research interests include high voltage technology and electromagnetic compatibility of power equipment.

Jiangping Lu received the M.S. degree in electrical engineering from the Xi'an Jiaotong University, Xi'an, China, in 1982.

He is currently working with the Power Research Institute, State Grid Shaanxi Electric Power Company Limited, Xi'an. His main research interests include high voltage instrument and electromagnetic compatibility of power equipment.

Dongxing Dou received the B.S. degree in electrical engineering in 2023 from the Xi'an University of Technology, Xi'an, China, where he is currently working toward the master's degree in electrical engineering.

His main research interests include electromagnetic compatibility simulation and test.